JCTC Journal of Chemical Theory and Computation

pubs.acs.org/JCTC Article

Microscopic Pressure Tensor in Cylindrical Geometry: Pressure of Water in a Carbon Nanotube

Kaihang Shi,* Yifan Shen, Erik E. Santiso,* and Keith E. Gubbins*

Cite This: J. Chem. Theory Comput. 2020, 16, 5548−5561 Read Online

ACCESS | Metrics & More | Article Recommendations | Supporting Information

ABSTRACT: The microscopic pressure tensor plays an important role in understanding the mechanical stability, transport, and high-pressure phenomena of confined phases. The lack of an exact formulation to account for the long-range Coulombic contribution to the local pressure tensor in cylindrical geometries prevents the characterization of molecular fluids confined in cylindrical pores. To address this problem, we first derive the local cylindrical pressure tensor for Lennard-Jones fluids based on the Harasima (H) definition, which is expected to be compatible with the Ewald summation method. The test of the H-definition pressure equations in a homogeneous system shows that the radial and azimuthal pressure have unphysical radial dependence near the origin, while the axial pressure gives physically meaningful values. We propose an alternative contour definition that is more appropriate for cylindrical geometry and show that it leads to physically realistic results for all three pressure tensor components. With this definition, the radial and azimuthal pressures are of Irving−Kirkwood (IK) type, and the axial pressure is of Harasima type. Because of the practical interest in the axial pressure, we develop a Harasima/Ewald (H/E) method for calculating the long-range Coulombic contribution to the local axial pressure for rigid molecules. As an application, the axial pressure profile of water inside and outside a (20, 20) single-wall carbon nanotube is determined. The H/E method is compared to the IK method, which assumes a spherically truncated Coulombic potential. Detailed analysis of the pressure profile by both methods shows that the water confined in the nanotube is in a stretched state overall in the axial direction.

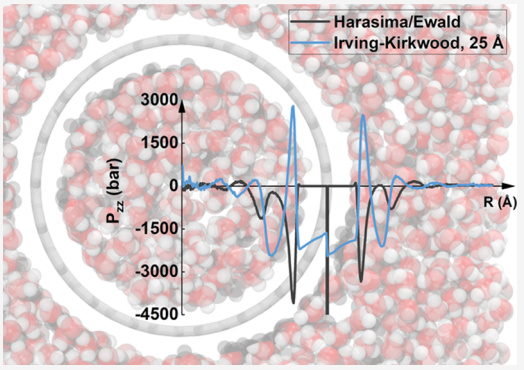

1. INTRODUCTION

The microscopic pressure tensor is key to understanding the mechanical stability of the thin films, such as lipid bilayers[1,2] and liquid film suspended in its vapor.[3] It also constitutes the virial route to the surface tension.[4−7] Conjectures based on the microscopic pressure help understand complicated phenomena, such as phase transitions[8−11] and some high-pressure chemical reactions[12,13] in highly inhomogeneous systems. Although it is very challenging to directly measure the microscopic pressure from experiments,[13,14] it is relatively straightforward to calculate this quantity from molecular simulations. The main difficulty associated with the local pressure tensor calculation is the nonuniqueness problem.[15,16] For pairwise interactions, the statistical formulation of the local pressure tensor depends on an arbitrary integral contour connecting two interacting particles.[16] This arbitrariness arises from the fact that there is no unique way to assign part of the nonlocal pair force to a local position. One widely used contour definition is that of Irving and Kirkwood (IK),[15,17] who defined the contour to be a straight line connecting two interacting particles. Alternative contour definitions are possible, a popular choice among which is the Harasima (H) definition.[4,17,18] The IK definition is naturally compatible with the pairwise interactions (e.g., van der Waals, Coulombic, and bonded interactions), and it can be readily extended to more complex molecular systems with many-body interactions (e.g., angular and dihedral) by decomposing the potential into pairwise components. This force decomposition is also not unique, and a number of dissection methods have been proposed.[1,19−22] For the H definition, the pressure only attributes to the position where the atom is located. Once the total force on an atom is known, the local pressure can be calculated.[2]

Another technical problem in calculating the local pressure tensor is how to correctly account for the long-range Coulombic interactions. The Coulombic interaction decays very slowly in space, and it is impossible to use a simple tail correction [as for the Lennard-Jones (LJ) potential] to account for the missing long-range part.[23] Scientists have spherically truncated (ST) the Coulombic potential with a large cutoff distance in the simulation box to calculate the pressure contribution from the

Received: June 13, 2020
Published: July 27, 2020

https://dx.doi.org/10.1021/acs.jctc.0c00607
J. Chem. Theory Comput. 2020, 16, 5548−5561

electrostatic interaction,[1,22,24] but such a treatment cannot guarantee a consistent pressure profile because the long-range Coulombic potential was treated differently (with Ewald-based method) in the molecular simulation and (with simple cutoff) in the pressure calculation. Better alternatives to this simple truncation of the Coulombic potential are the shifted-potential[25] and shifted-force[26] methods. In these methods, the bare Coulombic potential is replaced by a damped one, and the damped Coulombic potential is shifted to assure zero potential or force at the cutoff radius to create a neutral local environment of the central ion. Comparison with the Ewald-based method showed that the shifted-potential and shifted-force methods with appropriate damping parameter and cutoff radius can effectively reproduce the energetics and dynamics of various systems to an acceptable accuracy.[25,26] Nevertheless, the Ewald summation method[27] is still the standard method to compute long-range Coulombic interactions and to produce consistent results.[28] Hatch and Debenedetti[29] achieved the consistency of the Ewald method with the IK formulation by writing the Ewald sum in an explicit pairwise form. However, the Ewald sum in a pairwise form is very computationally expensive. In this case, the H definition is a better choice and it can be readily applied to the Ewald method in its efficient nonpairwise form (for the reciprocal space). Alejandre et al.[30] developed a formulation that uses the IK definition for the real space and the H definition for the reciprocal space. Later, Sonne et al.[2] used the H definition consistently in the Ewald method and extended the method for lipid bilayers. Recently, Sega et al.[31] improved the existing method using the more efficient mesh-based Ewald algorithm. All these developments, however, are for inhomogeneous systems with planar interfaces.

The statistical mechanical and computational formalism for the local pressure tensor have been well established for planar[2,5,16,32] and spherical[22,33−36] interfaces, but the theoretical development in a cylindrical geometry is generally overlooked. Lovett and coauthors[37,38] derived the local pressure at a cylindrical interface as the thermodynamic response to a local deformation of the boundary, which has some similarities to the H definition developed in Section 2.1. Their derived local pressure, however, is in a scalar form instead of a second-order tensor as it should be. Ten years later, Kim et al.[39] studied the properties of liquid threads and wrote out an expression for the local normal pressure following the IK definition, but unfortunately, they did not separate the azimuthal and axial pressure but instead treated both components as being the same. Recently, Addington et al.[40] provided a complete derivation for the local pressure tensor in a cylindrical geometry based on the IK definition. The cylindrical pressure tensor is not only important for the calculation of the surface tension of an interface having a cylindrical geometry[40] but would also help us to understand the mechanical stability of self-assembled micelles of a cylindrical shape[41,42] and the phase behavior and transport inside cylindrical nanopores. Most of the synthetized porous materials with a well-defined geometry have cylindrical or quasi-cylindrical pores, including carbon and silicon nanotubes, silica materials (e.g., MCM-41,[43] SBA-15,[44] and KIT-6[45,46]), and metal−organic frameworks [e.g., $(Ni_3(HITP)_2)$[47,48]].

In this work, to address the problem of calculating the microscopic pressure in the presence of the long-range Coulombic interactions in a cylindrical geometry, we first present, in Section 2, a derivation and a test of the local cylindrical pressure tensor for LJ fluids based on the H definition. This definition is expected to be compatible with the Ewald method as shown for planar geometries.[2,31] We note that while the H definition gives physically sensible results for the axial component of the pressure tensor for cylindrical geometries, both the radial and azimuthal pressure tensor components give unphysical results near the origin, as has been noted also for spherical geometries by Hafskjold and Ikeshoji.[35] As a valid alternative, we propose a new contour definition for the local cylindrical pressure tensor which retains the form of the radial and azimuthal pressures of the IK definition[40] but has the form of the axial pressure of the H definition. In many applications, the axial pressure is the most important quantity for investigating phase transitions,[49,50] phase behavior of confined materials,[11] and confined chemical reactions in nanoreactors.[12] The axial pressure is also necessary for calculating the fluid-wall surface tension,[51] for developing sophisticated equations of state for confined fluids,[24] and for designing efficient pressure/temperature-driven release systems using a nanotube as a container.[52,53] Therefore, in Section 3, a molecular expression for the local axial pressure component is derived for rigid molecules, which preserves the consistency of the Harasima-type axial pressure component with the Ewald summation method in cylindrical coordinates. As an application, we investigate the axial pressure variation of water inside and outside a single-wall carbon nanotube (SWCNT).

2. LJ FLUIDS

2.1. Cylindrical Pressure Tensor by the Harasima Definition. In cylindrical coordinates, (R, θ, z), if the fluid is under the condition of hydrostatic equilibrium, $\nabla\cdot\mathbf{P} = 0$, we have[40]

$$P_N = P_{RR}(R) \tag{1}$$

$$P_{T\theta} = P_{\theta\theta}(R) = P_N(R) + R\frac{dP_N(R)}{dR} \tag{2}$$

$$P_{Tz} = P_{zz}(R) \tag{3}$$

where P_{RR} is the normal pressure (N) in the radial direction, $P_{T\theta}$ is the tangential pressure (T) in the azimuthal direction, and P_{Tz} is the tangential pressure in the axial direction. There are two contributions to the total pressure tensor, the kinetic contribution, and the configurational contribution. The kinetic contribution to the pressure tensor is well defined and is given by $\mathbf{P}^{Kin}(R) = \rho(R)\, k_B T\mathbf{1}$, where $\rho(R)$ is the number density at radial position R, k_B is the Boltzmann constant, T is temperature, and $\mathbf{1}$ is the second-order unit tensor. For pairwise interactions, the configurational (C) pressure tensor is given by[17]

$$\mathbf{P}^C(\mathbf{r}) = \frac{1}{2}\left\langle \sum_{i\neq j} \mathbf{F}_{ij} \int_{C_{ij}} d\tilde{l}\,\delta(\mathbf{r} - \tilde{l}) \right\rangle \tag{4}$$

where $\langle ... \rangle$ is the ensemble average, $\mathbf{F}_{ij}$ is the force vector between the ij particle pair, and $\tilde{l}$ is a path vector integrated over the contour C_{ij}; the prefactor 1/2 is to account for double counting of particles. The integral contour C_{ij} is not uniquely defined. In the spirit of the H definition for the planar,[5,18] and later for the spherical interfaces,[33,35] here we design a Harasima integral path in a cylindrical geometry, and the path vector can be generally written as

$$\tilde{l} = (\alpha - 1)R_{ij}\hat{e}_{R,\theta_i} + R_j\hat{e}_{R,\theta_i+\beta\theta_{ij}} + (z_i + \gamma z_{ij})\hat{e}_z \tag{5}$$

https://dx.doi.org/10.1021/acs.jctc.0c00607
J. Chem. Theory Comput. 2020, 16, 5548−5561

where radial distance $R_{ij} = R_j - R_i$, azimuthal angle $\theta_{ij} = \theta_j - \theta_i$, and z-distance $z_{ij} = z_j - z_i$. Radial unit vectors $\hat{e}_{R,\theta_i}$, $\hat{e}_{R,\theta_i+\beta\theta_{ij}}$, and axial unit vector $\hat{e}_z$ are given by

$$\hat{e}_{R,\theta_i} = \begin{pmatrix} \cos\theta_i \\ \sin\theta_i \\ 0 \end{pmatrix} \qquad \hat{e}_{R,\theta_i+\beta\theta_{ij}} = \begin{pmatrix} \cos(\theta_i + \beta\theta_{ij}) \\ \sin(\theta_i + \beta\theta_{ij}) \\ 0 \end{pmatrix}$$

$$\hat{e}_z = \begin{pmatrix} 0 \\ 0 \\ 1 \end{pmatrix} \tag{6}$$

Parameters α, β, γ range from 0 to 1. If α, β, γ vary sequentially from 0 to 1, the path $\tilde{l}$ represents the contour C_{ij} in Figure 1. The

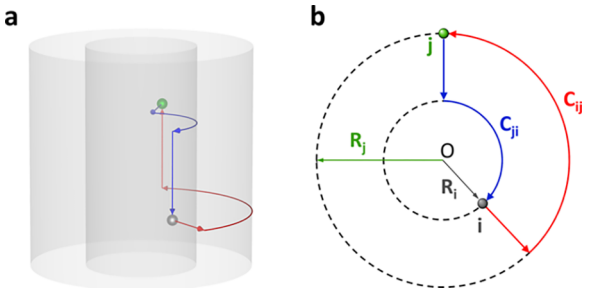

Figure 1. Harasima contour in cylindrical coordinates. The scheme is plotted in (a) a 3D view and (b) a top view (looking into the axial z-direction). The contour C_{ij} (in red) is composed of three separate paths: first, starting from particle i, (R_i, θ_i, z_i), to (R_j, θ_i, z_i), then to (R_j, θ_j, z_i), and eventually to the position of particle j, (R_j, θ_j, z_j). Particle i and particle j are indistinguishable; so, there is an equivalent contour C_{ji} (in blue) starting from particle j. The final pressure expression is the average from both contours.

nonsequential variation of α, β, γ will not alter the final expressions for the cylindrical pressure tensor. For simplicity, we will follow the case, where α, β, γ vary from 0 to 1, one by one. Differentiation of the vector $\tilde{l}$ gives a line element in cylindrical coordinates

$$d\tilde{l} = R_{ij}\hat{e}_{R,\theta_i}\, d\alpha + R_j\theta_{ij}\hat{e}_{\theta,\theta_i+\beta\theta_{ij}}\, d\beta + z_{ij}\hat{e}_z\, d\gamma \tag{7}$$

where the azimuthal unit vector $\hat{e}_{\theta,\theta_i+\beta\theta_{ij}}$ is

$$\hat{e}_{\theta,\theta_i+\beta\theta_{ij}} = \begin{pmatrix} -\sin(\theta_i + \beta\theta_{ij}) \\ \cos(\theta_i + \beta\theta_{ij}) \\ 0 \end{pmatrix} \tag{8}$$

We note that unlike the constant unit vectors in the Cartesian coordinate system, the radial and azimuthal unit vectors in cylindrical coordinates depend on the azimuthal angle θ. The delta function in eq 4 can be rewritten in a cylindrical form by

$$\delta(\mathbf{r} - \tilde{l}) = \frac{1}{R}\delta(R - R_l)\delta(\theta - \theta_l)\delta(z - z_l) \tag{9}$$

where $R_l = R_i + \alpha R_{ij}$ ($\alpha \in [0,1]$, $\beta = \gamma = 0$), $\theta_l = \theta_i + \beta\theta_{ij}$ ($\beta \in [0,1]$, $\alpha = 1$, $\gamma = 0$), and $z_l = z_i + \gamma z_{ij}$ ($\gamma \in [0,1]$, $\alpha = \beta = 1$) according to the designed contour. Using eq 9, we can rewrite eq 4 as

$$\mathbf{p}^{\mathrm{C}}(\mathbf{r}) = \frac{1}{2}\left\langle \sum_{i\neq j} \frac{\mathbf{r}_{ij}}{r_{ij}}\frac{1}{R}f_{ij}\int_{C_{ij}} d\tilde{l}\,\delta(R - R_l)\delta(\theta - \theta_l) \times \delta(z - z_l) \right\rangle \tag{10}$$

where vector $\mathbf{r}_{ij} = \mathbf{r}_j - \mathbf{r}_i$, r_{ij} is the scalar distance between the ij−pair, and f_{ij} is the ij−pair force for isotropic interactions.

We assume a cylinder having a height of L, and the cylinder height is related to the simulation box length L_z in the z-direction by $L = kL_z$, where $k \in (0,1]$. Starting from eqs 7 and 10, the diagonal elements of the second-order cylindrical pressure tensor can be determined with the result

$$P_{\mathrm{RR}}(R) = \rho(R)k_{\mathrm{B}}T + \frac{1}{4\pi R}\left\langle \sum_{i<j}(1 + \cos\theta_{ij})\frac{|R_{ij}|}{r_{ij}L}f_{ij}H(\alpha_1) \times H(1 - \alpha_1) \right\rangle \tag{11}$$

$$P_{\theta\theta}(R) = \rho(R)k_{\mathrm{B}}T + \frac{1}{4\pi R}\left\langle \sum_{i<j}[R_j\delta(R - R_j) + R_i\delta(R - R_i)](\hat{e}_{R,\theta_j} - \hat{e}_{R,\theta_i})\cdot\mathbf{r}_{ij}\frac{f_{ij}}{r_{ij}L} \right\rangle \tag{12}$$

$$P_{zz}(R) = \rho(R)k_{\mathrm{B}}T + \frac{1}{4\pi R}\left\langle \sum_{i<j}[\delta(R - R_j) + \delta(R - R_i)] \times \frac{z_{ij}^2}{r_{ij}L}f_{ij} \right\rangle \tag{13}$$

where $H(x)$ is the Heaviside step function ($x \geq 0$, $H(x) = 1$; $x < 0$, $H(x) = 0$), $\alpha_1 = (R - R_i)/R_{ij}$ for a given constant R-surface. Equation 13 is consistent with the eq 2.13 with $U_{ij} = z_{ij}^2$ in ref 38. A full derivation of eqs 11−13 is available in Section S1, Supporting Information. In practice, the delta function in the abovementioned equations can be approximated as

$$\delta(x - a) = \lim_{\xi\to 0}\frac{1}{\xi}H[x - (a - \xi/2)]H[(a + \xi/2) - x] \tag{14}$$

If we let $x = R$, $\xi = 2\Delta$, and $a = R_j$, eq 14 is equivalent to

$$\delta(R - R_j) = \lim_{\Delta\to 0}\frac{1}{2\Delta}H(R - R_j + \Delta)H(R_j + \Delta - R) \tag{15}$$

Replacing the delta functions in eqs 12 and 13 with the transformation in eq 15 will lead to expressions suitable for computer simulations.

2.2. Simulation details. We tested the cylindrical pressure tensor equations (eqs 11−13) in a bulk LJ fluid. The system was chosen to be LJ argon in its liquid state at $T = 100$ K and $P = 100$ bar. The molecular interactions were modeled by the 12-6 LJ potential

https://dx.doi.org/10.1021/acs.jctc.0c00607
J. Chem. Theory Comput. 2020, 16, 5548−5561

$$u^{\mathrm{LJ}}(r) = 4\varepsilon\left[\left(\frac{\sigma}{r}\right)^{12} - \left(\frac{\sigma}{r}\right)^{6}\right] \tag{16}$$

where r is the intermolecular distance; σ and ε are the molecular diameter and potential well depth, respectively, and were chosen to be σ = 3.405 Å and ε/k_B = 119.8 K. Molecular dynamics (MD) was implemented to model the system in the isothermal−isobaric (NPT) ensemble. The system contained N = 4000 LJ particles and had a box dimension of $L_x = L_y \sim 23\sigma$, $L_z \sim 9\sigma$. The box size was allowed to fluctuate during the simulation. A Nosé−Hoover-style thermostat/barostat was applied to maintain the imposed temperature and the pressure of the system. The temperature damping time and the pressure damping time were set to 0.2 and 2 ps, respectively. Periodic boundary conditions were applied in all directions. The system was integrated using the velocity Verlet algorithm. All simulations in this work were carried out using the LAMMPS (Large-scale Atomic/Molecular Massively Parallel Simulator, version 12 Dec 2018).[54]

To facilitate the simulation, the intermolecular potential was ST at the cutoff radius of $r_c = 3\sigma$

$$u_{\mathrm{ST}}(r) = \begin{cases} u^{\mathrm{LJ}}(r) & r \le r_c \\ 0 & r > r_c \end{cases} \tag{17}$$

where the potential is discontinuous at the cutoff radius; such an abrupt change in the potential value at r_c leads to an intermolecular force with an impulsive contribution at the cutoff radius[23,55−58]

$$f(r) = \begin{cases} -\dfrac{\mathrm{d}u^{\mathrm{LJ}}(r)}{\mathrm{d}r} + u_c\delta(r - r_c) & r \le r_c \\ 0 & r > r_c \end{cases} \tag{18}$$

where the term $u_c\delta(r - r_c)$ represents the impulsive force because of the discontinuity of the potential at r_c and $u_c = u^{\mathrm{LJ}}(r_c)$. Because the delta function in eq 18 is usually difficult to handle in the MD algorithm, most MD packages (including the LAMMPS used here) discard the impulsive force term, and the actual force evaluated during the simulation is

$$f(r) = \begin{cases} -\dfrac{\mathrm{d}u^{\mathrm{LJ}}(r)}{\mathrm{d}r} & r \le r_c \\ 0 & r > r_c \end{cases} \tag{19}$$

which essentially corresponds to the spherical truncated and shifted (STS) potential model[55]

$$u_{\mathrm{STS}}(r) = \begin{cases} u^{\mathrm{LJ}}(r) - u_c & r \le r_c \\ 0 & r > r_c \end{cases} \tag{20}$$

Therefore, the pair force f_{ij} in the pressure tensor expressions should be evaluated using eq 19 in the MD and we use eq 19 for the force calculations in this paper unless otherwise stated. As for the Monte Carlo (MC) simulation, no force evaluation is required. If the ST potential model is used in the MC simulation, the pair forces f_{ij} in the pressure tensor equations must be calculated by eq 18 and the impulsive force term should by no means be neglected. We observed that the failure of including the impulsive term in eq 18 when using the ST potential at $r_c = 3\sigma$ in a MC NPT simulation leads to a calculated pressure value of about 190 bar, compared to an imposed bulk pressure of 100 bar (almost 100% deviation).

We put the cylindrical coordinate system at the center of the simulation box, and the system was binned into cylindrical shells with the same radial thickness of about 0.01σ. When evaluating the delta function, the parameter Δ in eq 15 is chosen to be half of the cylindrical shell thickness, that is, $2\Delta \approx 0.01\sigma$. The simulation was performed for 20 ns with a timestep of 2 fs. The pressure tensor calculations were performed over the last 80,000 configurations.

2.3. Results and Discussion. In Figure 2 we show three diagonal components, P_{RR}, $P_{\theta\theta}$, and P_{zz}, in a bulk liquid LJ system. The radial pressure, P_{RR}, and the azimuthal pressure, $P_{\theta\theta}$, exhibit an unphysical radial dependence near the origin, while the axial pressure, P_{zz}, is a constant (within statistical errors), matching the imposed pressure (P = 100 bar) in the simulation. The anomalous behavior of the radial pressure near the origin is expected by examining eq 11. If we attempt to evaluate the configurational contribution (second term on the right of eq 11) of the radial pressure between a particle i at the center ($R_i = 0$) and a surrounding particle j at the radial position of R_j ($R_j > 0$), because of the cylindrical symmetry, we would expect that the ij-pair's contribution to P_{RR} is independent of the angle θ_{ij}. However, eq 11 shows dependence on θ_{ij} through the term $(1 + \cos\theta_{ij})$, indicating that some of the particles j at R_j contribute strongly to the radial pressure (when $\theta_{ij} \to 0$) and some of them contribute only weakly (when $\theta_{ij} \to \pi$); this is not rational on physical grounds. For the azimuthal pressure, we notice that the major difference between eq 12 and the (correct) eq 13 for the axial pressure is the presence of the radial distance R_i and R_j in front of the delta functions in eq 12. When a particle i is close to (or at) the center of the cylinder (i.e., $R_i \to 0$), eq 12 predicts a small (or zero) configurational contribution to the azimuthal pressure. This is confirmed by the fact that as $R \to 0$, both P_{RR} and $P_{\theta\theta}$ approximate the kinetic contribution to the pressure, $\rho k_B T$. When $R \gg 0$, both P_{RR} and $P_{\theta\theta}$ converge to the imposed pressure in the simulation.

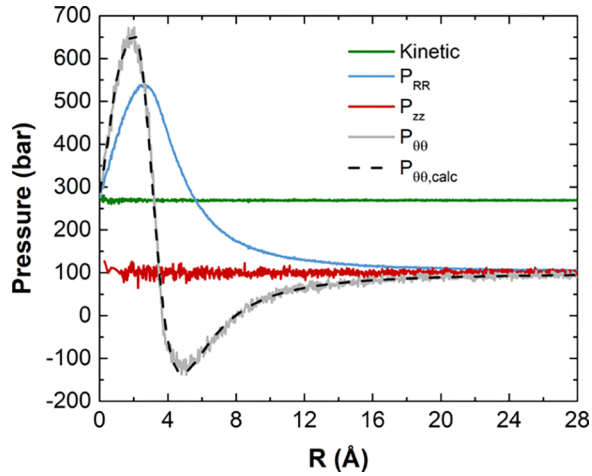

Figure 2. Radial profile of diagonal elements of the cylindrical pressure tensor by the Harasima definition in homogeneous liquid argon. The liquid was simulated in the isothermal−isobaric ensemble at T = 100 K and P = 100 bar. The radial (P_{RR}) and azimuthal ($P_{\theta\theta}$) components of the pressure tensor exhibit unphysical dependence on the radial distance near R = 0, but the axial component (P_{zz}) is a constant, as it should be. $P_{\theta\theta,\mathrm{calc}}$ was calculated from the hydrostatic equilibrium, that is, eq 2; the agreement between the simulation results and the calculated values confirms the consistency in our implementation.

https://dx.doi.org/10.1021/acs.jctc.0c00607
J. Chem. Theory Comput. 2020, 16, 5548−5561

Such unphysical radial dependence of the pressure in a bulk phase is because of a poor construction of the integral contour in polar coordinates. Similar to our case, unphysical radial dependence near the origin has also been observed for the local spherical pressure tensor using the H definition in a homogeneous hard-sphere fluid[35] and in LJ liquid droplets.[33] The local cylindrical pressure tensor following the IK definition was found to reflect the true pressure in homogeneous bulk fluids.[40] This is because the IK contour is defined as a straight line connecting two molecules, the construction of which is not associated with the polar coordinates (radial distance and polar angles). It should be noted that the singularity at the polar origin ($R = 0$) might be inevitable. It has been argued that the IK definition also suffers this abnormality at $R = 0$ in spherical coordinates.[59] Excluding the point at $R = 0$, the IK definition is preferred to the H definition in polar coordinates. However, from the preference for the IK contour, it should not be concluded that the IK definition of the local pressure tensor is uniquely correct in polar coordinates. Any construction of the integral contour that does not depend on the polar coordinates should be expected to be equally valid, as is the IK definition.

2.4. Alternative Pressure Definition for Cylindrical Geometry. In Figure 3, we propose an alternative contour for cylindrical geometry, which avoids the singularity near the origin of the H definition, while combining desirable features of both the IK and H definitions. The new contour vector is

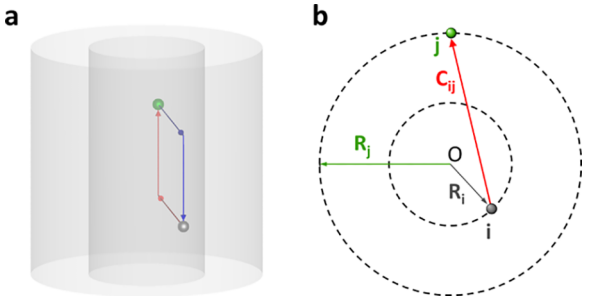

Figure 3. Alternative valid construction of the integral contour for the local pressure tensor in cylindrical coordinates. The scheme is plotted in (a) a 3D view and (b) a top view. The contour C_{ij} (in red) is composed of two separate paths: first starting from particle i (gray), (R_i, θ_i, z_i), horizontally to (R_j, θ_j, z_i), and then vertically to the position of particle j (green), (R_j, θ_j, z_j); the second path is the same as the final path of the Harasima contour defined in Figure 1. Because particle i and particle j are indistinguishable, the contour C_{ji} (blue line in the 3D view) is equivalent to C_{ij} (C_{ji} is not plotted in top view for clarity).

$$\tilde{l} = (1 - \alpha)R_i\hat{e}_{R,\theta_i} + \alpha R_j\hat{e}_{R,\theta_j} + (z_i + \beta z_{ij})\hat{e}_z \tag{21}$$

where parameters α and β vary sequentially from 0 to 1. The diagonal elements of the local cylindrical pressure tensor for this new contour are (see Section S2, Supporting Information, for derivation)

$$P_{RR}(R) = \rho(R)k_BT + \frac{1}{2\pi R}\left\langle \sum_{i<j}\sum_k \frac{|\mathbf{r}_{ij}\cdot\hat{e}_{R,\alpha_k}|}{r_{ij}L} f_{ij}H(\alpha_k) \times H(1 - \alpha_k)\right\rangle \tag{22}$$

$$P_{\theta\theta}(R) = \rho(R)k_BT + \frac{1}{2\pi R}\left\langle \sum_{i<j}\sum_k \frac{(\mathbf{r}_{ij}\cdot\hat{e}_{\theta,\alpha_k})^2}{|\mathbf{r}_{ij}\cdot\hat{e}_{R,\alpha_k}|} \times \frac{f_{ij}}{r_{ij}L}H(\alpha_k)H(1 - \alpha_k)\right\rangle \tag{23}$$

$$P_{zz}(R) = \rho(R)k_BT + \frac{1}{4\pi R}\left\langle \sum_{i<j}[\delta(R - R_j) + \delta(R - R_i)] \times \frac{z_{ij}^2}{r_{ij}L}f_{ij}\right\rangle \tag{24}$$

Equations 22 and 23 for the radial and azimuthal pressure components are equivalent to those of the IK definition[40] and so are well behaved. Most importantly, the result for the axial pressure, eq 24, is the same as the expression for this pressure component with the H definition (eq 13) and so is consistent with the Ewald summation method for long-range forces as shown in the next section. In eqs 22 and 23, α_k is the root of the equation $R^2 = (x_i + \alpha x_{ij})^2 + (y_i + \alpha y_{ij})^2$ and the unit vectors at $\alpha = \alpha_k$ are given by

$$\hat{e}_{R,\alpha_k} = \begin{pmatrix}(x_i + \alpha_k x_{ij})/R\\ (y_i + \alpha_k y_{ij})/R\\ 0\end{pmatrix} \qquad \hat{e}_{\theta,\alpha_k} = \begin{pmatrix}-(y_i + \alpha_k y_{ij})/R\\ (x_i + \alpha_k x_{ij})/R\\ 0\end{pmatrix} \tag{25}$$

We note that eq 23 has a different appearance than that in ref 40. Unlike the method in ref 40 that requires to take an average over a number of θ values in computation, here, we have already averaged over all possible θ analytically through integration (see eq S11). In the following sections, we focus on the axial pressure component because of the practical interest and extend eq 24 to complex systems of rigid molecules interacting with long-range Coulombic potential.

3. MOLECULAR FLUIDS

For a bulk fluid, the configurational part of the pressure tensor can be calculated by the virial theorem[60]

$$VP^C_{\alpha\beta} = \left\langle \sum_i r_i^\alpha f_i^\beta \right\rangle \tag{26}$$

where V is the volume of the system, $P^C_{\alpha\beta}$ is the pressure tensor component representing the force per unit area in the β-direction acting on a surface element normal to the α-direction; r_i^α is the position of particle i in the α-direction, and f_i^β is the total force exerted on particle i in the β-direction. Equation 26 is the most general form of calculating the configurational contribution to the bulk (i.e., spatially averaged) pressure tensor of the system, and it is the so-called atomic representation of the pressure tensor.[61,62] Equation 26 involves the net force on each atom arising from all interaction potentials, including pairwise interactions (e.g., bonded and nonbonded), three-body interactions (e.g., angle-bending), four-body interactions (e.g., dihedral and improper) and higher-body interactions. The constraint force, imposed by the SHAKE algorithm,[63] for example, should also be included in the force calculations.[1,62] The derivation of the local version for the atomic pressure tensor

https://dx.doi.org/10.1021/acs.jctc.0c00607
J. Chem. Theory Comput. 2020, 16, 5548−5561

is straightforward, depending on the criteria to dissect the force in space.[19−21] An alternative is the molecular representation of the pressure tensor.[61,62] The molecular pressure tensor takes the molecule as a whole, and no intramolecular contribution to the pressure is accounted for. This molecular representation is particularly suitable for rigid molecules and avoids calculating virial contributions from rigid constraints. The molecular pressure tensor has been applied to study the surface tension and pressure profile across the vapor−liquid interface.[30,64]

3.1. Local Axial Pressure with ST Coulombic Interactions. For rigid molecules interacting with the ST LJ and Columbic potentials, the molecular representation of eq 4 is given by

$$\mathbf{P}^{\mathrm{C}}(\mathbf{r}) = \frac{1}{2}\left\langle \sum_{i\neq j}\sum_{a}\sum_{b}\mathbf{F}_{iajb}\int_{C_{ij}} \mathrm{d}\tilde{l}\,\delta(\mathbf{r}-\tilde{l})\right\rangle \tag{27}$$

where $\mathbf{F}_{iajb}$ is the force vector between atom a in molecule i and atom b in molecule j and C_{ij} now is defined as an arbitrary contour connecting the center of mass (COM) of two interacting molecules. For the IK definition, the contour is a straight line, $\tilde{l} = \mathbf{r}_i + \alpha\mathbf{r}_{ij}$ with $\alpha \in [0,1]$, and the configurational contribution to the local axial pressure is given by

$$P^{\mathrm{C}}_{zz,\mathrm{IK}}(R) = \frac{1}{2\pi R}\left\langle \sum_{i<j}\sum_{a}\sum_{b}\sum_{k}\frac{z_{ij}z_{iajb}}{|\mathbf{r}_{ij}\cdot\hat{e}_{R,\alpha_k}|}\times\frac{f_{iajb}}{r_{iajb}L}H(\alpha_k) \times H(1-\alpha_k)\right\rangle \tag{28}$$

where $z_{iajb} = z_{jb} - z_{ia}$; r_{iajb} and f_{iajb} are the scalar distance and force between the atom a in molecule i and the atom b in molecule j, respectively; α_k is the root of $R^2 = (x_i + \alpha x_{ij})^2 + (y_i + \alpha y_{ij})^2$ at a given R-surface; the radial unit vector $\hat{e}_{R,\alpha_k}$ at $\alpha = \alpha_k$ is given by

$$\hat{e}_{\mathrm{R},\alpha_k} = \begin{pmatrix} (x_i + \alpha_k x_{ij})/R \\ (y_i + \alpha_k y_{ij})/R \\ 0 \end{pmatrix} \tag{29}$$

It is assumed in Equation 28 that two interacting molecules are both within the defined cylinder of height L. In cases where part of the straight-line contour is inside the defined cylinder, the valid solutions are those for $z_l(\alpha_k)$ inside the defined cylinder. For the Harasima-type axial pressure component (Figure 3), the molecular version of the configurational part in eq 24 is given by

$$P^{\mathrm{C}}_{zz,\mathrm{H}}(R) = \frac{1}{4\pi R}\left\langle \sum_{i<j}\sum_{a}\sum_{b}\frac{z_{ij}z_{iajb}}{r_{iajb}L}f_{iajb}[\delta(R-R_j) + \delta(R-R_i)]\right\rangle \tag{30}$$

3.2. Local Axial Pressure with Ewald Summation Method. The calculation of the bulk pressure tensor with the Ewald summation method[27] is well established in the field.[61,65] The total electrostatic energy can be written by the Ewald summation method[66] as

$$U^{\mathrm{ELE}} = \sum_{i<j}\sum_{a}\sum_{b}\frac{q_{ia}q_{jb}[\mathrm{erfc}(\kappa r_{iajb})/r_{iajb}]}{4\pi\varepsilon_0} + \frac{1}{2V\varepsilon_0} \times \sum_{\mathbf{h}\neq 0}\frac{1}{h^2}\exp\left(-\frac{h^2}{4\kappa^2}\right)S(\mathbf{h})S(-\mathbf{h}) - \frac{\kappa}{\sqrt{\pi}}\sum_{i}\sum_{a}\frac{q_{ia}^2}{4\pi\varepsilon_0} - \sum_{i}\sum_{a}\sum_{b>a}\frac{q_{ia}q_{ib}}{4\pi\varepsilon_0}\frac{\mathrm{erf}(\kappa r_{iaib})}{r_{iaib}} + \frac{1}{2\varepsilon_0(2\varepsilon_s+1)V}\left|\sum_{i}\sum_{a}q_{ia}\mathbf{r}_{ia}\right|^2 \tag{31}$$

where ε_0 is the permittivity of vacuum; κ is the damping parameter, the introduction of which assures the convergence of the Coulombic energy in the real space; $\mathrm{erfc}(x)$ is the complementary error function and $\mathrm{erfc}(x) = 1 - \mathrm{erf}(x)$. The box volume is $V = L_xL_yL_z$, and the reciprocal space (i.e., Fourier space) vector $\mathbf{h}$ is defined as $\mathbf{h} = (2\pi n_x/L_x, 2\pi n_y/L_y, 2\pi n_z/L_z)$ with n_x, n_y, and n_z taking integer values. The structure factor is given by

$$S(\mathbf{h}) = \sum_{j}\sum_{b}q_{jb}\exp(i\mathbf{h}\cdot\mathbf{r}_{jb}) \tag{32}$$

The first term on the right of eq 31 accounts for the real space contribution, the second on the right is the contribution from the reciprocal space, the third term corrects the spurious self-interaction in the reciprocal space, and the fourth term corrects the intramolecular energy for small rigid molecules. The last term on the right of eq 31 is the surface term[67] which accounts for the dipole moment on the sphere of box replicas that is embedded in a surrounding medium with relative permittivity (dielectric constant) of ε_s.[66] If $\varepsilon_s = \infty$, as is assumed in the Ewald method and was applied throughout in the current work, the surface term vanishes, and this is called the conducting ("tin-foil") boundary condition. If there is no surrounding medium ($\varepsilon_s = 1$, vacuum) as is the case for the direct lattice sum, the surface term cannot be simply neglected (see example in Appendix A in ref 29). It is clear from eq 31 that writing the energy in the reciprocal space in a pairwise form is very inefficient. Instead, we write out the electrostatic energy for molecule i in the reciprocal space (K) with the self-correction term as

$$\begin{aligned} U_i^{\mathrm{K}} &= \frac{1}{2V\varepsilon_0}\sum_{\mathbf{h}\neq 0}\frac{1}{h^2}\exp\left(-\frac{h^2}{4\kappa^2}\right)\left[S(\mathbf{h})\sum_{a}q_{ia}\exp(-i\mathbf{h}\cdot\mathbf{r}_{ia}) + S(-\mathbf{h})\sum_{a}q_{ia}\exp(i\mathbf{h}\cdot\mathbf{r}_{ia})\right] - \frac{\kappa}{\sqrt{\pi}}\sum_{a}\frac{q_{ia}^2}{4\pi\varepsilon_0} \\ &= \frac{1}{V\varepsilon_0}\sum_{\mathbf{h}\neq 0}\frac{1}{h^2}\exp\left(-\frac{h^2}{4\kappa^2}\right)\sum_{a}q_{ia}\mathrm{Re}[\exp(-i\mathbf{h}\cdot\mathbf{r}_{ia})S(\mathbf{h})] - \frac{\kappa}{\sqrt{\pi}}\sum_{a}\frac{q_{ia}^2}{4\pi\varepsilon_0} \end{aligned} \tag{33}$$

where the function $\mathrm{Re}(x)$ extracts the real part of a complex number. We note that eq 33 contains the intramolecular interactions in the reciprocal space.

Once having the potential energy, to derive the molecular pressure tensor, it would be convenient to start from the thermodynamic definition of the pressure. In a canonical ensemble for example, the bulk (scalar) pressure is defined as

https://dx.doi.org/10.1021/acs.jctc.0c00607
J. Chem. Theory Comput. 2020, 16, 5548−5561

$$P = -\left(\frac{\partial A}{\partial V}\right)_{N,T} \tag{34}$$

where A is the Helmholtz free energy. By substituting $A = -k_B T \ln Q$ into eq 34, where Q is the total partition function of the system, and after simple manipulations, we have

$$P = \rho k_B T - \left\langle \frac{\partial U}{\partial V} \right\rangle_{N,T} \tag{35}$$

where U is the total configurational energy of the system. If we approximate the partial derivative in eq 35 by a finite volume expansion, we obtain the thermodynamic route (also known as the volume perturbation method) to the pressure.[57,68,69] Equation 35 is exact, and we can directly extend it to the calculation of the local pressure tensor. For a cylinder with height L in the axial direction, we can divide the cylinder into several shells with equal radial thickness of 2Δ, where Δ is a finite number but is small enough and is near zero. Based on eq 35, the local axial pressure in the cylindrical shell located at R is given by

$$P_{zz}(R) = \rho(R) k_B T - \frac{1}{4\pi R\Delta}\left\langle \frac{\partial U(R)}{\partial L} \right\rangle \tag{36}$$

where $\rho(R)$ is the molecular density profile; $U(R)$ is the potential energy in the cylindrical slab at a radial distance of R. Different criteria of assigning potential energy in slabs will lead to different local pressure values,[70] again suggesting that there is no unique definition of the local pressure tensor. Here, we adopt the choice of Ladd and Woodcock[71] and only assign the potential energy into the slab if any one of the interacting molecules involved is in that slab; this choice corresponds to the Harasima-type axial pressure component in the new contour definition in Figure 3.

Having selected the criterion to assign the local potential energy, the total potential energy in a cylindrical shell is given by

$$U(R) = U^{LJ}(R) + U^{R}(R) + U^{K}(R) + U^{intra}(R) \tag{37}$$

where the LJ potential is

$$U^{LJ}(R) = \frac{1}{2}\sum_{i\neq j}\sum_{a}\sum_{b} u^{LJ}(r_{iajb}) H(R - R_i + \Delta) \times H(R_i + \Delta - R) \tag{38}$$

the electrostatic potential in the real space (R) is

$$U^{R}(R) = \frac{1}{2}\sum_{i\neq j}\sum_{a}\sum_{b} \frac{q_{ia}q_{jb}}{4\pi\varepsilon_0}\frac{\mathrm{erfc}(\kappa r_{iajb})}{r_{iajb}} H(R - R_i + \Delta) \times H(R_i + \Delta - R) \tag{39}$$

the electrostatic potential in the reciprocal space (K) is

$$U^{K}(R) = \frac{1}{2}\sum_{i} U_i^{K} H(R - R_i + \Delta) H(R_i + \Delta - R) \tag{40}$$

and the last term correcting the electrostatic intramolecular interactions is

$$U^{intra}(R) = -\sum_{i}\sum_{a}\sum_{b>a} \frac{q_{ia}q_{ib}}{4\pi\varepsilon_0}\frac{\mathrm{erf}(\kappa r_{iaib})}{r_{iaib}} H(R - R_i + \Delta) \times H(R_i + \Delta - R) \tag{41}$$

Now, substituting eqs 37 into 36 results in

$$\begin{aligned} P_{zz,H}(R) &= \rho(R)k_B T - \frac{1}{4\pi R\Delta}\left\langle \frac{\partial U^{LJ}(R)}{\partial L} + \frac{\partial U^{R}(R)}{\partial L} + \frac{\partial U^{K}(R)}{\partial L} + \frac{\partial U^{intra}(R)}{\partial L} \right\rangle \\ &= \rho(R)k_B T + P_{zz,H}^{LJ}(R) + P_{zz,H}^{R}(R) + P_{zz,H}^{K}(R) + P_{zz,H}^{intra}(R) \end{aligned} \tag{42}$$

The LJ pressure component, $P_{zz,H}^{LJ}(R)$, takes the same form as eq 30. It is easy to see that $\partial U^{intra}(R)/\partial L = 0$ for rigid molecules, and thus, $P_{zz,H}^{intra}(R) = 0$. Substituting eqs 39 into 42 gives the local axial pressure because of the electrostatic interactions in the real space

$$\begin{aligned} P_{zz,H}^{R}(R) &= -\frac{1}{8\pi R\Delta}\left\langle \sum_{i\neq j}\sum_{a}\sum_{b} \frac{q_{ia}q_{jb}}{4\pi\varepsilon_0}\frac{\partial[\mathrm{erfc}(\kappa r_{iajb})/r_{iajb}]}{\partial r_{iajb}} \frac{\partial r_{iajb}}{\partial L_z}\frac{\partial L_z}{\partial L} H(R - R_i + \Delta) H(R_i + \Delta - R) \right\rangle \\ &= \frac{1}{4\pi R}\left\langle \sum_{i\neq j}\sum_{a}\sum_{b} \frac{q_{ia}q_{jb}}{4\pi\varepsilon_0}\left[\frac{2\kappa\,\exp(-\kappa^2 r_{iajb}^2)}{\sqrt{\pi}\, r_{iajb}} + \frac{\mathrm{erfc}(\kappa r_{iajb})}{r_{iajb}^2}\right]\frac{z_{ij}z_{iajb}}{r_{iajb}L}\delta(R - R_i) \right\rangle \end{aligned} \tag{43}$$

where in the last step, we used eq 15 to convert the Heaviside step functions to the delta function. While carrying out the partial derivative of $\partial r_{iajb}/\partial L_z$, we note that the scaled COM distance, $s_{ij} = z_{ij}/L_z$, and the intramolecular distance, $\mathbf{d}_{ia} = \mathbf{r}_{ia} - \mathbf{r}_i$, are both invariant to the volume scaling. Combining eqs 33, 40, and 42 yields the equation for the local axial pressure coming from the reciprocal space

$$P_{zz,H}^{K}(R) = -\frac{1}{8\pi R\Delta}\left\langle \sum_{i} \frac{\partial U_i^{K}}{\partial L} H(R - R_i + \Delta) \times H(R_i + \Delta - R) \right\rangle \tag{44}$$

where

$$\begin{aligned} \frac{\partial U_i^{K}}{\partial L} = \frac{\partial U_i^{K}}{\partial L_z}\frac{\partial L_z}{\partial L} &= -\frac{1}{V\varepsilon_0 L}\sum_{\mathbf{h}\neq 0}\frac{1}{h^2}\exp\left(-\frac{h^2}{4\kappa^2}\right) \times \sum_{a} q_{ia}\,\mathrm{Re}[\exp(-i\mathbf{h}\cdot\mathbf{r}_{ia})S(\mathbf{h})] \\ &\times \left[1 - 2h_z^2\left(\frac{1}{h^2} + \frac{1}{4\kappa^2}\right)\right] \\ &+ \frac{1}{V\varepsilon_0 L}\sum_{\mathbf{h}\neq 0}\frac{1}{h^2}\exp\left(-\frac{h^2}{4\kappa^2}\right)h_z\sum_{a} q_{ia} \\ &\times \mathrm{Re}[id_{ia,z}\exp(-i\mathbf{h}\cdot\mathbf{r}_{ia})S(\mathbf{h}) - i\exp(-i\mathbf{h}\cdot\mathbf{r}_{ia})Q(\mathbf{h})] \end{aligned} \tag{45}$$

and

$$Q(\mathbf{h}) = \sum_{j}\sum_{b} q_{jb} d_{jb,z}\exp(i\mathbf{h}\cdot\mathbf{r}_{jb}) \tag{46}$$

https://dx.doi.org/10.1021/acs.jctc.0c00607
J. Chem. Theory Comput. 2020, 16, 5548−5561

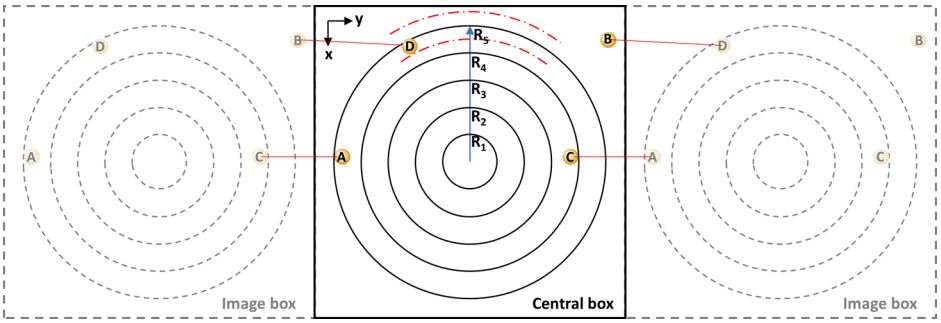

Figure 4. Illustration of the local axial pressure calculations in a cylindrical geometry under periodic boundary conditions. The axial direction of the cylinder is perpendicular to the *xy* plane. In the central box, the red dash-dotted line indicates the boundary of the thin cylindrical shell located at R_5, for example. For the IK definition, the A−C interaction contributes twice to the local axial pressure at R_5 and once at R_4; the B−D interaction contributes only once to the local axial pressure at R_5. For the Harasima (H) definition, the A−C interaction contributes half to the local axial pressure in the cylindrical shell located at R_5 and half to the shell at R_4; the B−D interaction only contributes half to the shell at R_5 because the particle (or center of mass of the molecule) B is outside the sampling region ($0 \le R_{sample} \le R_5 + \Delta$) where the pressure will be calculated.

In eq 45, $h_z = 2\pi n_z/L_z$ and the intramolecular distance $d_{ia,z} = z_{ia} - z_i$. Averaging the summation of eqs 43 and 44 over the defined cylinder geometry having a radius of R_c, that is, $\bar{P}_{zz} = 2\int_0^{R_c} [P^R_{zz,H}(r) + P^K_{zz,H}(r)]r\, dr/{R_c}^2$, leads to the Coulombic component of the bulk (spatially averaged) axial pressure expression that is in agreement with eq A10 in ref 30. However, in ref 30, the authors distributed the reciprocal space contribution equally to each molecule, which is an unjustified assumption for highly inhomogeneous systems.[31] The above derivation of the reciprocal space contribution to the local axial pressure is similar to the scenario for planar geometry. In that case, following the H definition, the reciprocal-space pressure contribution from molecule/atom *i* can be explicitly derived and it is assigned to the planar slab where the molecule/atom is located.[2] Equation 42 and its contributing parts (eqs 30, 43, and 44) constitute the Harasima/Ewald (H/E) method for the local axial pressure in a cylindrical geometry.

3.3. Simulation Details. We first tested our molecular pressure equations in a bulk system with 2500 water molecules at T = 300 K and P = 100 bar in the *NPT* ensemble. The water model was chosen to be the rigid SPC/E model[72] with the SHAKE algorithm[63] applied for bond and angle constraints. A Nose−Hoover-style thermostat/barostat was applied with the temperature damping time and the pressure damping time of 0.1 and 1 ps, respectively. Periodic boundary conditions were applied in all directions. To calculate the pressure tensor under periodic boundary conditions, the particle−particle interaction in the central box (unit cell) and the particle−image interaction across the box boundary should both be accounted for.[73] Figure 4 illustrates the rules of accounting for the particle−image interactions in the pressure calculation by both IK and H definition. The cutoff radius for the LJ interactions was set to 10 Å. The long-range electrostatic interactions were handled by the particle−particle particle−mesh method.[66,74] The damped Coulombic interaction in the real space was cut off at 10 Å with a damping parameter κ of 0.3077 Å^{-1}. The grid size in the reciprocal space was adjusted during the simulation based on the instantaneous box dimensions, damping parameter, and computation accuracy (absolute accuracy was set to 10^{-5} eV/Å). The cylindrical sampling region was divided into cylindrical shells with thickness of 0.05 Å. The system was equilibrated for 2 ns with a timestep of 1 fs, and the local axial pressure was post-calculated over 1.2×10^6 configurations from the subsequent 60 ns production run.

Once validated, the developed molecular pressure equations are used to calculate the axial pressure profile for SPC/E water inside and outside a (20, 20) SWCNT. The SWCNT is a 6 nm-long tube with a diameter of 2.712 nm, having the "armchair" configuration. The nanotube was kept rigid during the simulation by setting the net force on each carbon atom to zero. The center of the SWCNT was fixed at the center of the simulation box, and the axial direction was aligned with the *z*-axis of the box. The carbon atoms (C) in the SWCNT were assumed to be neutral and interact only with the oxygen atom (O) in the water molecule through the 12-6 LJ potential. The carbon−oxygen LJ parameters were taken from Werder et al.,[75] that is, ε_{CO}/k_B = 47.147 K and σ_{CO} = 3.19 Å. LJ and Coulombic interactions were handled in the same way as in the bulk water simulations. At the beginning, an empty nanotube was placed in a water bath having 11,000 water molecules under periodic boundary conditions. An *NVT* run was first performed for 100 ps to gradually heat the system up to 300 K, and an equilibrium *NPT* run was immediately followed for another 2 ns with a timestep of 1 fs. The temperature and the (hydrostatic) pressure of the system were kept at 300 K and 1 atm, respectively. Only the center-of-mass positions of the water molecules were scaled during the *NPT* run. The water filled the initially empty SWCNT within 1 ns, consistent with the previous observations.[76] An equilibrated configuration of the system is shown in Figure 5. The local axial pressure was post-calculated over 1.6×10^6 configurations from the subsequent 40 ns production run. The pressure sampling was only performed at the middle of the

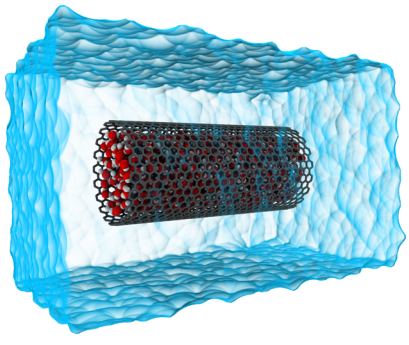

Figure 5. Typical simulation snapshot for a (20, 20) SWCNT submerged in a water bath after equilibrium. The water molecules outside the SWCNT are not shown for clarity.

https://dx.doi.org/10.1021/acs.jctc.0c00607
J. Chem. Theory Comput. 2020, 16, 5548−5561

SWCNT, and the pore edge effect is negligible. The source code for pressure analysis is available at https://github.com/KaihangShi/Cylindrical-Pressure-Tensor.

3.4. Results and Discussion. *3.4.1. Bulk Water.* To validate our H/E implementation, we calculated the local axial pressure in a bulk water system assuming a cylindrical geometry. As a result, the H/E method leads to an axial pressure profile that fluctuates around the imposed pressure in the *NPT* simulation across the whole system (see Figure 6). In addition to the H/E method, the IK method (e.g., eq 28 for the configurational contribution) was also used to evaluate the local axial pressure, assuming the Coulombic interaction is simply truncated in the simulation box. The IK method, however, yields axial pressure profiles that depend on the Coulombic cutoff distance (see Figure 6). The averages of the local data shown in Figure 6 are summarized in Table 1. In general, the new H/E method can reproduce the bulk pressure controlled by the barostat (i.e., P = 100 bar). For the IK method with Coulombic interactions cutoff at r_{elec} = 10 Å, the averaged pressure is not even close to the imposed bulk pressure and is a negative value. When we increase the Coulombic cutoff radius up to 18 Å, which is limited by the box dimension, the averaged bulk pressure by the IK method shows a nonmonotonic trend that slowly converges to the imposed bulk pressure. We expect that the IK result will eventually agree with the H/E result if the cutoff radius is large enough (providing the simulation box is also large enough) so that the Coulombic energy can converge within the unit cell. The results in Table 1 support the conclusion that the H/E method is preferred, and it gives a reliable pressure value that reflects the true state of a homogeneous system or of a homogeneous region in an inhomogeneous system (see Section 3.4.2). This preference does not imply that the H/E method is more correct than the IK method with the pairwise Ewald sum or with the direct lattice sum,[29] but the H/E method clearly has advantages in its computational efficiency.

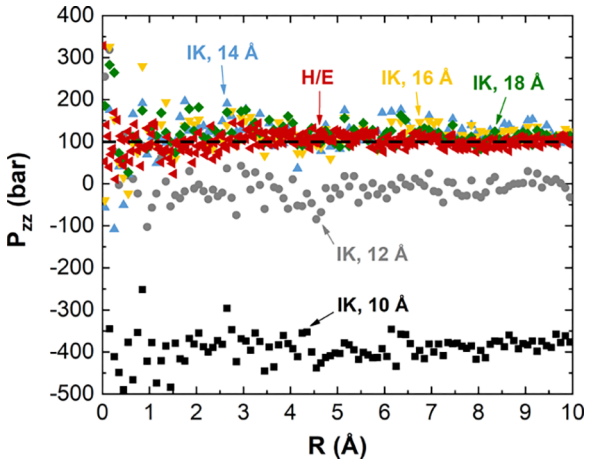

Figure 6. Radial profile of the local axial pressure by the IK method and by the H/E method in bulk water. The liquid water was simulated in the isothermal−isobaric (*NPT*) ensemble at T = 300 K and P = 100 bar. Because the IK method assumes a ST Coulombic potential in the box, the resulting pressure profiles are dependent on the cutoff distance. The axial pressure calculated by the H/E method fluctuates around the imposed *NPT* pressure (P = 100 bar, black dashed line), confirming the consistency in our H/E implementation.

Table 1. Averaged Axial Pressure in Bulk Water Simulated in the Isothermal−Isobaric Ensemble at T = 300 K and P = 100 bar[a]

method	r_{elec} (Å)	P_{zz} (bar)
H/E	10	100.8 ± 11.4
IK	10	−388.3 ± 18.5
	12	−6.7 ± 18.0
	14	125.4 ± 21.5
	16	120.9 ± 16.5
	18	113.9 ± 17.6

[a]The IK method, assuming the Coulombic interactions are simply truncated at a distance (r_{elec}), is compared with the accurate H/E method. The pressure values presented here are composed of the average of the local axial pressure and the standard error. For better statistics, the average was carried out for $R \geq 5$ Å in Figure 6.

To better understand each contributing part in the H/E method, we decompose the total pressure into the kinetic, short-range, and reciprocal-space contributions in Table 2. The short-range part includes both the LJ and the real-space-damped Coulombic interactions. When the damped Coulombic interaction is truncated in real space at 10 Å, the contribution from the reciprocal space accounts for ∼24% with respect to the total pressure. If we keep the computational accuracy of the Ewald method the same and take a longer Coulombic cutoff in the real space, r_{elec} = 18 Å (with κ = 0.17094 Å^{-1}), the contribution from the reciprocal space now only accounts for ∼1%. This is a consequence of how we split the Coulombic energy in the Ewald method.[2] In the latter case, the real-space contribution plays a major role in the total Coulombic energy and the systematic error introduced by replacing the bare Coulombic potential with a damped one is small.[25]

Table 2. Decomposition of the Total Axial Pressure of the Bulk Water by the H/E Method into the Kinetic Part (P^{Kin}), Short-range Part ($P^{LJ}_{zz,H} + P^{R}_{zz,H}$), and the Reciprocal-space Part ($P^{K}_{zz,H}$)[a]

r_{elec} (Å)	P^{Kin} (bar)	$P^{LJ}_{zz,H} + P^{R}_{zz,H}$ (bar)	$P^{K}_{zz,H}$ (bar)	P_{zz} (bar)
10	1374.7 ± 1.2	−1249.9 ± 10.7	−24.0 ± 2.2	100.8 ± 11.4
18	1374.3 ± 1.8	−1272.7 ± 16.3	−1.1 ± 1.3	100.6 ± 16.5

[a]The bulk system was simulated in the isothermal−isobaric ensemble at T = 300 K and P = 100 bar. The damped Coulombic interaction in the real space is cut off at two different values (r_{elec}), but the overall Ewald accuracy is kept the same and is consistent with the simulation setup. The pressure values are composed of the average of the local axial pressure and the standard error. For better statistics, the average was carried out for $R \geq 5$ Å.

3.4.2. Water Confined in a (20, 20) SWCNT. Here, we illustrate an application of the new H/E method in investigating the axial pressure profile of water inside and outside a (20, 20) SWCNT, having an internal radius of 1.356 nm. For the pressure contributions from fluid−wall (fw) interactions, the atomic representation of the pressure tensor has been adopted because defining a COM position for a solid material is usually insensible, especially when such solid is modeled as an "infinitely" large one under the periodic boundary conditions.[62] The fw contribution to the local axial pressure by the IK and by the H definition is given by

https://dx.doi.org/10.1021/acs.jctc.0c00607
J. Chem. Theory Comput. 2020, 16, 5548−5561

$$P_{zz,\mathrm{IK}}^{\mathrm{fw}}(R) = \frac{1}{2\pi R}\left\langle \sum_i \sum_a \sum_b \sum_k \frac{z_{ib}z_{iab}}{|\mathbf{r}_{ib}\cdot\hat{e}_{R,\alpha_k}|} \times \frac{f_{iab}}{r_{iab}L} H(\alpha_k) \times H(1-\alpha_k) \right\rangle \quad (47)$$

$$P_{zz,\mathrm{H}}^{\mathrm{fw}}(R) = \frac{1}{4\pi R}\left\langle \sum_i \sum_a \sum_b \frac{z_{ib}z_{iab}}{r_{iab}L} f_{iab}[\delta(R-R_b) + \delta(R-R_i)] \right\rangle \quad (48)$$

where the summation is over all water molecules i and atoms a inside the water molecule and over all carbon atoms b in the modeled SWCNT. Equation 28 is similar to eq 47 here with the subscript jb (or j) replaced by b; the distance $z_{ib} = z_b - z_i$ and $z_{iab} = z_b - z_{ia}$. To derive eqs 47 and 48, we realize that the carbon atoms in the SWCNT are scaled with the volume transformation in the axial direction (see Appendix in ref 62). In this case, the intramolecular carbon−carbon (wall−wall) interactions (e.g., bonded and angle) will contribute to the local pressure tensor. Because we simply kept the nanotube rigid in this work, the wall−wall contribution to the local axial pressure is not considered here.

The local axial pressure and density of water inside and outside the SWCNT is shown in Figure 7. The axial pressure profile by the H/E method is compared with those by the IK method at two different Coulombic cutoff radii, r_{elec} = 15 and 25 Å. Increasing the cutoff distance from 15 to 25 Å does not make visually significant changes to the whole IK axial pressure profile, but it is discernible that the bulk pressure outside the nanotube is slowly converged to the exact value by the H/E method. The true bulk pressure simulated outside the nanotube is about 30 bar higher than the imposed pressure (1 atm) in the *NPT* simulation. This is because the current *NPT* algorithm was designed to control the hydrostatic pressure (one-third of the trace of the pressure tensor) of a homogeneous system. In other words, this algorithm maintains the hydrostatic pressure of the whole system and has no control over the pressure in a specific region of an inhomogeneous system (e.g., the bulk region outside the SWCNT). In general, we observed only a minor confinement effect on the pressure profile because of the large diameter of the nanotube. The axial pressure profile inside the nanotube is very similar to that outside for both methods and we expect bigger differences between the pressure profile inside and outside as the tube diameter decreases. For the pressure profile by the H/E method, the axial pressure is negative overall and presents negative peaks at the peak positions in the density profile (see Figure 7, bottom panel). The local axial pressure in the first and the second water layer (near the wall) inside the nanotube dips to about −4100 and −1100 bar, respectively. The negative pressure pulse at R = 13.56 Å (the radial position of the nanotube wall, see Figure 7, upper panel) is because the attractive forces between water molecules and the nanotube wall, and the H definition assigns the pressure to the position of the wall atoms. The IK pressure profile, unlike that by the H/E method, is in phase with the density profile, presenting enhanced pressure peaks at the position of the water layers (as high as 2800 bar) and pressure drops (as low as −2400 bar) between two layers. Because the IK definition assigns the force in space between the two interacting molecules, there is no negative pressure pulse at the position of the nanotube wall. We have also calculated the axial pressure profile by the H definition with the Coulombic potential treated in the same way as in the IK method (i.e., ST Coulombic potential at r_{elec} = 25 Å). We found that the axial pressure profile by the H definition is almost identical to that by the H/E method (data not shown), indicating that the significant difference in results between the IK and H/E method as shown in Figure 7 should be attributed to the difference in contour definitions for the local pressure, instead of the different ways to treat the Coulombic interactions. It is worth noting that neither the H/E nor the IK pressure profile resembles the results reported by Barati Farimani and Aluru.[77] The authors[77] reported a "local pressure" of 1000 bar near the center of a (20, 20) carbon nanotube at room temperature and pressure. This pressure is suspected because the authors incorrectly used the virial equation for the scalar pressure to calculate the local pressure tensor in an inhomogeneous phase. A similar mistake was also made in ref 78.

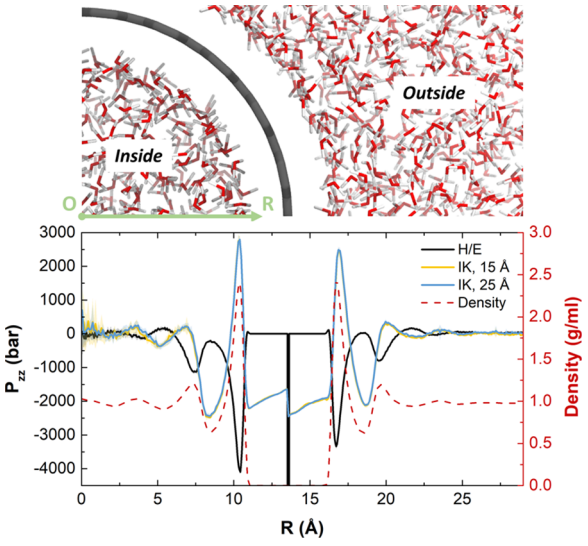

Figure 7. Upper panel: a cross-sectional snapshot of water inside and outside of a (20, 20) SWCNT. Bottom panel: local axial pressure (including both fluid−fluid and fw contributions) vs the radial distance from the center of the SWCNT. The H/E method is compared with the IK method at two different Coulombic cutoff radii. These two IK profiles are almost indistinguishable in the region of $R \in (5, 20)$. The molecular density profile of water is also plotted. The shaded area in the pressure profile denotes the standard error. The upper-panel snapshot is plotted in the same radial length scale as in the bottom-panel pressure profile.

To better understand the intermolecular interactions behind the pressure profiles, the total pressure is decomposed into the fluid−fluid (including kinetic contribution) and fw contributions in Figure 8. For both the H/E and IK methods, the fluid−fluid pressure profile shows a positive peak in the first water layer near the nanotube wall, and the pressure peak by the IK method is sharper and higher than that of the H/E method. This positive pressure peak is because of the accumulation of the water molecules near the wall. The attractive force field provided by the carbon wall pulls the water molecules toward the wall and the crowded environment in the first adsorbed layer leads to the compression between the water molecules. The decomposition of the fluid−fluid pressure profile into each contributing force reveals that the pressure enhancement in the first layer results from the kinetic energy and LJ overlaps. We note that the

https://dx.doi.org/10.1021/acs.jctc.0c00607
J. Chem. Theory Comput. 2020, 16, 5548−5561

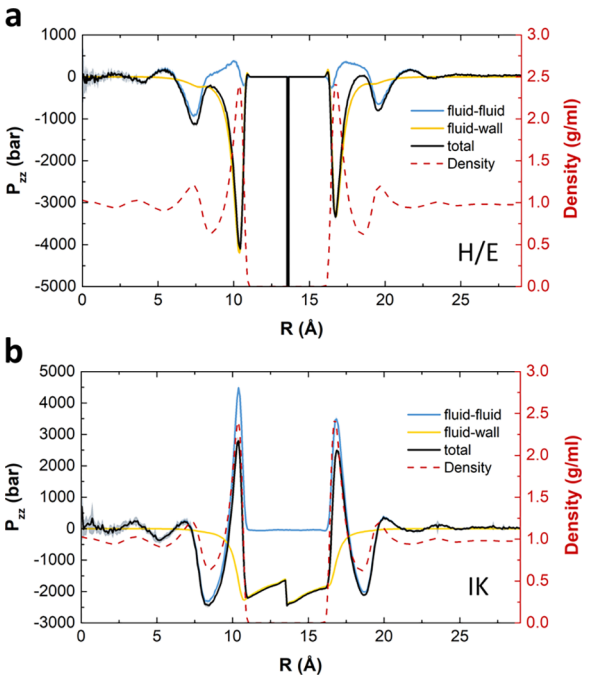

Figure 8. Decomposition of the local axial pressure (in Figure 7) (a) by the H/E method and (b) by the IK method, into the fluid−fluid and fw contributions. The kinetic contribution is included in the fluid−fluid profile. For the IK method, the Coulombic interaction is ST at 25 Å. The molecular density profile of water inside and outside the nanotube is also plotted. The shaded area in the pressure profile denotes the standard error.

pressure enhancement in this case is much smaller than the tangential pressure of the argon-adsorbed layer on a carbon surface;[40,79−82] this is because argon has stronger wetting behavior than water with carbon. Moreover, a negative fluid−fluid pressure peak is observed in the second adsorbed water layer in the H/E scenario, indicating that the second water layer experiences the strong attractive interactions. In the IK scenario, because the force is assigned in the space between the interacting pair, the prominent negative peak is observed between the first and the second water layer, implying that the two layers are in tension. This negative pressure is mainly because of the electrostatic attraction from the first adsorbed water layer (the fluid−fluid LJ contribution to the pressure is always positive in the water phase). A negative tangential pressure having a similar order of magnitude was also found in water confined by two parallel hydrophobic walls.[8] However, the pressure reported in ref 8 was the averaged pressure over the whole pore, and it is not clear if the fw contribution was accounted for. Two small negative peaks are also observed in the fluid−fluid axial pressure profile in the vicinity of the nanotube wall by the H/E method, suggesting the water molecules inside the nanotube weakly attract the water molecules outside. This observation is consistent with the fluid−fluid pressure profile by the IK method, where a slightly negative pressure is present at the radial distance from 11 to 16 Å. If the fluid−fluid contribution to the local axial pressure in Figure 8 is spatially averaged over the entire cylindrical pore, we will have a very similar in-pore pressure for both the H/E method (∼−36 bar) and the IK method (∼−33 bar), where the small differences in value might be a result of the insufficient cutoff radius used for the Coulombic potential in the IK method. This negative in-pore pressure indicates that the confined water is in a stretched state overall in the axial direction. In addition to the fluid−fluid contributions, both H/E and IK methods lead to a negative fw axial pressure profile inside and outside the nanotube because of the attractive potential field exerted by the carbon wall. The fw pressure profile gradually decays to zero near the pore center and toward the bulk, following the decaying behavior of the attractive external potential exerted on the water molecules by the carbon wall.

4. CONCLUSIONS

The long-range Coulombic contribution to the local pressure tensor is essential to the understanding of the physical properties of complex systems. Past efforts have incorporated the Ewald summation method into the calculation of the long-range contribution to the local pressure in inhomogeneous systems having planar interfaces,[2,30,31] but no efficient formulation has been proposed for cylindrical geometries so far. To achieve this goal, we have first proposed the Harasima (H) definition for the local pressure tensor in a system having a cylindrical interface based on the original H definition for planar geometry[5,18] and on the later development in spherical coordinates.[33,35] We chose the H definition here because it has been proven compatible with the Ewald sum in an efficient nonpairwise form for systems of planar geometry.[2,31] The equations for diagonal elements of the cylindrical pressure tensor have been derived for LJ spheres and were tested in a homogeneous LJ system. Similar to the situation in spherical coordinates,[35] the calculated pressure profile shows that the radial and azimuthal pressure components have unphysical radial dependence near the origin, while only the axial pressure gives a physically meaningful value, in agreement with the imposed pressure in the isothermal−isobaric MD simulation. The results confirm that, in general, the H definition is not appropriate in cylindrical coordinates, in contrast to the IK definition.[40] We have proposed a valid alternative to the H definition for cylindrical geometries that gives physically meaningful results for all three pressure components. The new contour definition retains the Harasima expression for the axial pressure component, which is suitable for use with the Ewald summation method to treat long-range Coulombic interactions. In general, we suggest that any construction of the integral contour for the local pressure tensor that depends on the polar coordinates (i.e., radius and polar angles) should be avoided.

Because of the recent increased interest in the axial pressure for fluids confined in different cylindrical pores, we have presented a H/E method to calculate the long-range Coulombic contributions to the local axial pressure for rigid molecules based on the Ewald summation algorithm and the Harasima-type axial pressure component. As an application, we implemented our approach to investigate the axial pressure profile for water inside and outside a (20, 20) SWCNT in a water bath. The H/E method is compared to the IK method, which assumes a ST Coulombic potential. The two definitions lead to distinct local axial pressure profiles near the pore wall, reflecting the nonunique nature of the local pressure tensor, but they consistently show a pressure profile that approaches the bulk value near the tube center and far outside. The detailed analysis of the fluid−fluid contribution to the axial pressure reveals that the first water layer near the wall is in compression because of the accumulation of the water molecules adjacent to the attractive carbon wall. The first water layer then attracts the second adsorbed water layer next to it through the electrostatic interactions, creating tension between these two layers. The

https://dx.doi.org/10.1021/acs.jctc.0c00607
J. Chem. Theory Comput. 2020, 16, 5548−5561

spatial average of the fluid−fluid contribution to the local axial pressure over the entire cylindrical pore indicates that the confined water is in a stretched state. We have also accounted for the fw contribution to the pressure. Because of the attractive force field provided by the carbon wall, the fw interactions contribute negatively to the axial pressure over the entire radial range. Adding up both fluid−fluid and fw contributions to the local axial pressure, however, leads to a seemingly inconsistent mechanical picture for the first adsorbed water layer between the H/E and IK method. The two methods produce opposite pressure peaks corresponding to the first layer in the density profile (i.e., a negative pressure peak for the H/E method and a positive pressure peak for the IK method). This confusion points to the need to explore the possibility of developing a unique definition of the microscopic pressure,[83,84] which could provide a holistic and well-defined picture of the system. A study on this topic is in progress.

The correct implementation of the pressure calculation is important for understanding the mechanical and thermodynamic state of the system. The method developed in this work can be used to study transport phenomena of fluids in cylindrical pores and to investigate the hydrogen-bond-induced pressurization (or hydrophobic hydration effect) in confinement.[85] The calculation of the local pressure in an inhomogeneous system can also act as a safety check to ensure that the bulk-like region in the system is correctly simulated at the desired conditions.

■ ASSOCIATED CONTENT

Supporting Information

The Supporting Information is available free of charge at https://pubs.acs.org/doi/10.1021/acs.jctc.0c00607.

Full derivation of the cylindrical pressure tensor for LJ fluids based on the Harasima and the new contour definitions (PDF)

■ AUTHOR INFORMATION

Corresponding Authors

Kaihang Shi − *Department of Chemical & Biomolecular Engineering, North Carolina State University, Raleigh, North Carolina 27606, United States;* orcid.org/0000-0002-0297-1746; Email: kshi3@ncsu.edu

Erik E. Santiso − *Department of Chemical & Biomolecular Engineering, North Carolina State University, Raleigh, North Carolina 27606, United States;* orcid.org/0000-0003-1768-8414; Email: eesantis@ncsu.edu

Keith E. Gubbins − *Department of Chemical & Biomolecular Engineering, North Carolina State University, Raleigh, North Carolina 27606, United States;* orcid.org/0000-0001-6760-5897; Email: keg@ncsu.edu

Author

Yifan Shen − *Department of Chemistry, Johns Hopkins University, Baltimore, Maryland 21218, United States*

Complete contact information is available at: https://pubs.acs.org/10.1021/acs.jctc.0c00607

Notes

The authors declare no competing financial interest.

■ ACKNOWLEDGMENTS

The authors thank Cody Addington and Harold ("Wick") Hatch for helpful discussions. This work was supported by the U.S. National Science Foundation under grant no. CBET-1603851.

■ REFERENCES

(1) Vanegas, J. M.; Torres-Sánchez, A.; Arroyo, M. Importance of Force Decomposition for Local Stress Calculations in Biomembrane Molecular Simulations. *J. Chem. Theory Comput.* **2014**, *10*, 691−702.

(2) Sonne, J.; Hansen, F. Y.; Peters, G. H. Methodological Problems in Pressure Profile Calculations for Lipid Bilayers. *J. Chem. Phys.* **2005**, *122*, 124903.

(3) Weng, J.-G.; Park, S.; Lukes, J. R.; Tien, C.-L. Molecular Dynamics Investigation of Thickness Effect on Liquid Films. *J. Chem. Phys.* **2000**, *113*, 5917−5923.

(4) Kirkwood, J. G.; Buff, F. P. The Statistical Mechanical Theory of Surface Tension. *J. Chem. Phys.* **1949**, *17*, 338−343.

(5) Walton, J. P. R. B.; Tildesley, D. J.; Rowlinson, J. S.; Henderson, J. R. The Pressure Tensor at the Planar Surface of a Liquid. *Mol. Phys.* **1983**, *48*, 1357−1368.

(6) Ibergay, C.; Ghoufi, A.; Goujon, F.; Ungerer, P.; Boutin, A.; Rousseau, B.; Malfreyt, P. Molecular Simulations of the N-Alkane Liquid-Vapor Interface: Interfacial Properties and Their Long Range Corrections. *Phys. Rev. E: Stat., Nonlinear, Soft Matter Phys.* **2007**, *75*, 051602.

(7) Shi, K.; Lian, C.; Bai, Z.; Zhao, S.; Liu, H. Dissipative Particle Dynamics Study of the Water/Benzene/Caprolactam System in the Absence or Presence of Non-Ionic Surfactants. *Chem. Eng. Sci.* **2015**, *122*, 185−196.

(8) Giovambattista, N.; Rossky, P. J.; Debenedetti, P. G. Phase Transitions Induced by Nanoconfinement in Liquid Water. *Phys. Rev. Lett.* **2009**, *102*, 050603.

(9) Fujimori, T.; Morelos-Gómez, A.; Zhu, Z.; Muramatsu, H.; Futamura, R.; Urita, K.; Terrones, M.; Hayashi, T.; Endo, M.; Young Hong, S.; Chul Choi, Y.; Tománek, D.; Kaneko, K. Conducting Linear Chains of Sulphur inside Carbon Nanotubes. *Nat. Commun.* **2013**, *4*, 2162.

(10) Urita, K.; Shiga, Y.; Fujimori, T.; Iiyama, T.; Hattori, Y.; Kanoh, H.; Ohba, T.; Tanaka, H.; Yudasaka, M.; Iijima, S.; Moriguchi, I.; Okino, F.; Endo, M.; Kaneko, K. Confinement in Carbon Nanospace-Induced Production of KI Nanocrystals of High-Pressure Phase. *J. Am. Chem. Soc.* **2011**, *133*, 10344−10347.

(11) Addington, C. K.; Mansell, J. M.; Gubbins, K. E. Computer Simulation of Conductive Linear Sulfur Chains Confined in Carbon Nanotubes. *Mol. Simul.* **2017**, *43*, 519−525.

(12) Srivastava, D.; Turner, C. H.; Santiso, E. E.; Gubbins, K. E. The Nitric Oxide Dimer Reaction in Carbon Nanopores. *J. Phys. Chem. B* **2018**, *122*, 3604−3614.

(13) Vasu, K. S.; Prestat, E.; Abraham, J.; Dix, J.; Kashtiban, R. J.; Beheshtian, J.; Sloan, J.; Carbone, P.; Neek-Amal, M.; Haigh, S. J.; Geim, A. K.; Nair, R. R. Van Der Waals Pressure and Its Effect on Trapped Interlayer Molecules. *Nat. Commun.* **2016**, *7*, 12168.

(14) Templer, R. H.; Castle, S. J.; Rachael Curran, A.; Rumbles, G.; Klug, D. R. Sensing Isothermal Changes in the Lateral Pressure in Model Membranes Using Di-Pyrenyl Phosphatidylcholine. *Faraday Discuss.* **1999**, *111*, 41−53.

(15) Irving, J. H.; Kirkwood, J. G. The Statistical Mechanical Theory of Transport Processes. IV. The Equations of Hydrodynamics. *J. Chem. Phys.* **1950**, *18*, 817−829.

(16) Schofield, P.; Henderson, J. R. Statistical Mechanics of Inhomogeneous Fluids. *Proc. R. Soc. A Math. Phys. Eng. Sci.* **1982**, *379*, 231−246.

(17) Gray, C. G.; Gubbins, K. E.; Joslin, C. G. Sec. 8.3 Pressure Tensor. In *Theory of Molecular Fluids. Vol. 2: Applications*; Oxford University Press, 2011; pp 928−942.

(18) Harasima, A. Molecular Theory of Surface Tension. In *Advances in Chemical Physics*; Wiley & Sons, Inc., 1958; Vol. *64*, pp 203−237.

(19) Goetz, R.; Lipowsky, R. Computer Simulations of Bilayer Membranes: Self-Assembly and Interfacial Tension. *J. Chem. Phys.* **1998**, *108*, 7397−7409.
(20) Heinz, H.; Paul, W.; Binder, K. Calculation of Local Pressure Tensors in Systems with Many-Body Interactions. *Phys. Rev. E: Stat., Nonlinear, Soft Matter Phys.* **2005**, *72*, 066704.
(21) Admal, N. C.; Tadmor, E. B. A Unified Interpretation of Stress in Molecular Systems. *J. Elast.* **2010**, *100*, 63−143.
(22) Nakamura, T.; Shinoda, W.; Ikeshoji, T. Novel Numerical Method for Calculating the Pressure Tensor in Spherical Coordinates for Molecular Systems. *J. Chem. Phys.* **2011**, *135*, 094106.
(23) Frenkel, D.; Smit, B. *Understanding Molecular Simulation: From Algorithms to Applications*, 2nd ed.; Academic Press: San Diego, 2002.
(24) Sadeghi, M.; Parsafar, G. A. Toward an Equation of State for Water inside Carbon Nanotubes. *J. Phys. Chem. B* **2012**, *116*, 4943−4951.
(25) Wolf, D.; Keblinski, P.; Phillpot, S. R.; Eggebrecht, J. Exact Method for the Simulation of Coulombic Systems by Spherically Truncated, Pairwise R−1 Summation. *J. Chem. Phys.* **1999**, *110*, 8254−8282.
(26) Fennell, C. J.; Gezelter, J. D. Is the Ewald Summation Still Necessary? Pairwise Alternatives to the Accepted Standard for Long-Range Electrostatics. *J. Chem. Phys.* **2006**, *124*, 234104.
(27) Ewald, P. P. Die Berechnung Optischer Und Elektrostatischer Gitterpotentiale. *Ann. Phys.* **1921**, *369*, 253−287.
(28) Perera, L.; Essmann, U.; Berkowitz, M. L. Effect of the Treatment of Long-range Forces on the Dynamics of Ions in Aqueous Solutions. *J. Chem. Phys.* **1995**, *102*, 450−456.
(29) Hatch, H. W.; Debenedetti, P. G. Molecular Modeling of Mechanical Stresses on Proteins in Glassy Matrices: Formalism. *J. Chem. Phys.* **2012**, *137*, 035103.
(30) Alejandre, J.; Tildesley, D. J.; Chapela, G. A. Molecular Dynamics Simulation of the Orthobaric Densities and Surface Tension of Water. *J. Chem. Phys.* **1995**, *102*, 4574−4583.
(31) Sega, M.; Fábián, B.; Jedlovszky, P. Pressure Profile Calculation with Mesh Ewald Methods. *J. Chem. Theory Comput.* **2016**, *12*, 4509−4515.
(32) Rao, M.; Berne, B. J. On the Location of Surface of Tension in the Planar Interface between Liquid and Vapour. *Mol. Phys.* **1979**, *37*, 455−461.
(33) Thompson, S. M.; Gubbins, K. E.; Walton, J. P. R. B.; Chantry, R. A. R.; Rowlinson, J. S. A Molecular Dynamics Study of Liquid Drops. *J. Chem. Phys.* **1984**, *81*, 530−542.
(34) Tjatjopoulos, G. J.; Mann, J. A. The Pressure Tensor of an Inhomogeneous Fluid. *Mol. Phys.* **1987**, *60*, 1425−1432.
(35) Hafskjold, B.; Ikeshoji, T. Microscopic Pressure Tensor for Hard-Sphere Fluids. *Phys. Rev. E: Stat., Nonlinear, Soft Matter Phys.* **2002**, *66*, 011203.
(36) Ikeshoji, T.; Hafskjold, B.; Furuholt, H. Molecular-Level Calculation Scheme for Pressure in Inhomogeneous Systems of Flat and Spherical Layers. *Mol. Simul.* **2003**, *29*, 101−109.
(37) Lovett, R.; Baus, M. A Molecular Theory of the Laplace Relation and of the Local Forces in a Curved Interface. *J. Chem. Phys.* **1997**, *106*, 635−644.
(38) Mareschal, M.; Baus, M.; Lovett, R. The Local Pressure in a Cylindrical Liquid−Vapor Interface: A Simulation Study. *J. Chem. Phys.* **1997**, *106*, 645−654.
(39) Kim, B. G.; Lee, J. S.; Han, M.; Park, S. A Molecular Dynamics Study on Stability and Thermophysical Properties of Nanoscale Liquid Threads. *Nanoscale Microscale Thermophys. Eng.* **2006**, *10*, 283−304.
(40) Addington, C. K.; Long, Y.; Gubbins, K. E. The Pressure in Interfaces Having Cylindrical Geometry. *J. Chem. Phys.* **2018**, *149*, 084109.
(41) Wang, X.; Guerin, G.; Wang, H.; Wang, Y.; Manners, I.; Winnik, M. A. Cylindrical Block Copolymer Micelles and Co-Micelles of Controlled Length and Architecture. *Science* **2007**, *317*, 644−647.
(42) Qiu, H.; Hudson, Z. M.; Winnik, M. A.; Manners, I. Multidimensional Hierarchical Self-Assembly of Amphiphilic Cylindrical Block Comicelles. *Science* **2015**, *347*, 1329−1332.
(43) Kresge, C. T.; Leonowicz, M. E.; Roth, W. J.; Vartuli, J. C.; Beck, J. S. Ordered Mesoporous Molecular Sieves Synthesized by a Liquid-Crystal Template Mechanism. *Nature* **1992**, *359*, 710−712.
(44) Zhao, D.; Feng, J.; Huo, Q.; Melosh, N.; Fredrickson, G. H.; Chmelka, B. F.; Stucky, G. D. Triblock Copolymer Syntheses of Mesoporous Silica with Periodic 50 to 300 Angstrom Pores. *Science* **1998**, *279*, 548−552.
(45) Kleitz, F.; Hei Choi, S.; Ryoo, R. Cubic Ia3d Large Mesoporous Silica: Synthesis and Replication to Platinum Nanowires, Carbon Nanorods and Carbon NanotubesElectronic Supplementary Information (ESI) Available: TEM Images of Mesoporous Cubic Silica and Pt Networks, XRD Patterns during Forma. *Chem. Commun.* **2003**, 2136.
(46) Kleitz, F.; Bérubé, F.; Guillet-Nicolas, R.; Yang, C.-M.; Thommes, M. Probing Adsorption, Pore Condensation, and Hysteresis Behavior of Pure Fluids in Three-Dimensional Cubic Mesoporous KIT-6 Silica. *J. Phys. Chem. C* **2010**, *114*, 9344−9355.
(47) Bi, S.; Banda, H.; Chen, M.; Niu, L.; Chen, M.; Wu, T.; Wang, J.; Wang, R.; Feng, J.; Chen, T.; Dincă, M.; Kornyshev, A. A.; Feng, G. Molecular Understanding of Charge Storage and Charging Dynamics in Supercapacitors with MOF Electrodes and Ionic Liquid Electrolytes. *Nat. Mater.* **2020**, *19*, 552−558.
(48) Sheberla, D.; Bachman, J. C.; Elias, J. S.; Sun, C.-J.; Shao-Horn, Y.; Dincă, M. Conductive MOF Electrodes for Stable Supercapacitors with High Areal Capacitance. *Nat. Mater.* **2017**, *16*, 220−224.
(49) Koga, K.; Gao, G. T.; Tanaka, H.; Zeng, X. C. Formation of Ordered Ice Nanotubes inside Carbon Nanotubes. *Nature* **2001**, *412*, 802−805.
(50) Mochizuki, K.; Koga, K. Solid−liquid Critical Behavior of Water in Nanopores. *Proc. Natl. Acad. Sci.* **2015**, *112*, 8221−8226.
(51) Hamada, Y.; Koga, K.; Tanaka, H. Phase Behavior and Fluid−Solid Surface Tension of Argon in Slit Pores and Carbon Nanotubes. *Phys. A Stat. Mech. its Appl.* **2009**, *388*, 2289−2298.
(52) Chaban, V. V.; Prezhdo, V. V.; Prezhdo, O. V. Confinement by Carbon Nanotubes Drastically Alters the Boiling and Critical Behavior of Water Droplets. *ACS Nano* **2012**, *6*, 2766−2773.
(53) Chaban, V. V.; Prezhdo, O. V. Pressure-Driven Opening of Carbon Nanotubes. *Nanoscale* **2016**, *8*, 6014−6020.
(54) Plimpton, S. Fast Parallel Algorithms for Short-Range Molecular Dynamics. *J. Comput. Phys.* **1995**, *117*, 1−19.
(55) Trokhymchuk, A.; Alejandre, J. Computer Simulations of Liquid/Vapor Interface in Lennard-Jones Fluids: Some Questions and Answers. *J. Chem. Phys.* **1999**, *111*, 8510−8523.
(56) Martínez-Ruiz, F. J.; Blas, F. J.; Mendiboure, B.; Moreno-Ventas Bravo, A. I. Effect of Dispersive Long-Range Corrections to the Pressure Tensor: The Vapour-Liquid Interfacial Properties of the Lennard-Jones System Revisited. *J. Chem. Phys.* **2014**, *141*, 184701.
(57) de Miguel, E.; Jackson, G. The Nature of the Calculation of the Pressure in Molecular Simulations of Continuous Models from Volume Perturbations. *J. Chem. Phys.* **2006**, *125*, 164109.
(58) Allen, M. P.; Tildesley, D. J. Sec. 5 Some Tricks of the Trade. *Computer Simulation of Liquids*, 2nd ed.; Oxford University Press, 2017; Vol. *1*.
(59) Sodt, A. J.; Pastor, R. W. The Tension of a Curved Surface from Simulation. *J. Chem. Phys.* **2012**, *137*, 234101.
(60) Allen, M. P.; Tildesley, D. J. Sec. 2.7 Time Correlation Functions and Transport Coefficients. *Computer Simulation of Liquids*, 2nd ed.; Oxford University Press, 2017; Vol. *1*.
(61) Heyes, D. M. Pressure Tensor of Partial-Charge and Point-Dipole Lattices with Bulk and Surface Geometries. *Phys. Rev. B: Condens. Matter Mater. Phys.* **1994**, *49*, 755−764.
(62) Brown, D.; Neyertz, S. A General Pressure Tensor Calculation for Molecular Dynamics Simulations. *Mol. Phys.* **1995**, *84*, 577−595.
(63) Ryckaert, J.-P.; Ciccotti, G.; Berendsen, H. J. C. Numerical Integration of the Cartesian Equations of Motion of a System with Constraints: Molecular Dynamics of n-Alkanes. *J. Comput. Phys.* **1977**, *23*, 327−341.
(64) Ghoufi, A.; Goujon, F.; Lachet, V.; Malfreyt, P. Surface Tension of Water and Acid Gases from Monte Carlo Simulations. *J. Chem. Phys.* **2008**, *128*, 154716.

https://dx.doi.org/10.1021/acs.jctc.0c00607
J. Chem. Theory Comput. 2020, 16, 5548−5561

(65) Nosé, S.; Klein, M. L. Constant Pressure Molecular Dynamics for Molecular Systems. *Mol. Phys.* **1983**, *50*, 1055−1076.
(66) Allen, M. P.; Tildesley, D. J. Sec. 6 Long-Range Forces. *Computer Simulation of Liquids*, 2nd ed.; Oxford University Press, 2017; Vol. *1*.
(67) de Leeuw, S. W.; Perram, J. W.; Smith, E. R. Simulation of Electrostatic Systems in Periodic Boundary Conditions. I. Lattice Sums and Dielectric Constants. *Proc. R. Soc. London. A. Math. Phys. Sci.* **1980**, *373*, 27−56.
(68) Harismiadis, V. I.; Vorholz, J.; Panagiotopoulos, A. Z. Efficient Pressure Estimation in Molecular Simulations without Evaluating the Virial. *J. Chem. Phys.* **1996**, *105*, 8469−8470.
(69) Eppenga, R.; Frenkel, D. Monte Carlo Study of the Isotropic and Nematic Phases of Infinitely Thin Hard Platelets. *Mol. Phys.* **1984**, *52*, 1303−1334.
(70) Long, Y.; Palmer, J. C.; Coasne, B.; Śliwinska-Bartkowiak, M.; Jackson, G.; Müller, E. A.; Gubbins, K. E. On the Molecular Origin of High-Pressure Effects in Nanoconfinement: The Role of Surface Chemistry and Roughness. *J. Chem. Phys.* **2013**, *139*, 144701.
(71) Ladd, A. J. C.; Woodcock, L. V. Interfacial and Co-Existence Properties of the Lennard-Jones System at the Triple Point. *Mol. Phys.* **1978**, *36*, 611−619.
(72) Berendsen, H. J. C.; Grigera, J. R.; Straatsma, T. P. The Missing Term in Effective Pair Potentials. *J. Phys. Chem.* **1987**, *91*, 6269−6271.
(73) Heinz, H. Calculation of Local and Average Pressure Tensors in Molecular Simulations. *Mol. Simul.* **2007**, *33*, 747−758.
(74) Hockney, R. W.; Eastwood, J. W. *Computer Simulation Using Particles*; Hilger: Bristol, 1988.
(75) Werder, T.; Walther, J. H.; Jaffe, R. L.; Halicioglu, T.; Koumoutsakos, P. On the Water−Carbon Interaction for Use in Molecular Dynamics Simulations of Graphite and Carbon Nanotubes. *J. Phys. Chem. B* **2003**, *107*, 1345−1352.
(76) Pascal, T. A.; Goddard, W. A.; Jung, Y. Entropy and the Driving Force for the Filling of Carbon Nanotubes with Water. *Proc. Natl. Acad. Sci.* **2011**, *108*, 11794−11798.
(77) Barati Farimani, A.; Aluru, N. R. Existence of Multiple Phases of Water at Nanotube Interfaces. *J. Phys. Chem. C* **2016**, *120*, 23763−23771.
(78) Faraji, F.; Rajabpour, A. Temperature Gradient-Induced Fluid Pumping inside a Single-Wall Carbon Nanotube: A Non-Equilibrium Molecular Dynamics Study. *Phys. Fluids* **2016**, *28*, 092004.
(79) Gubbins, K. E.; Gu, K.; Huang, L.; Long, Y.; Mansell, J. M.; Santiso, E. E.; Shi, K.; Śliwińska-Bartkowiak, M.; Srivastava, D. Surface-Driven High-Pressure Processing. *Engineering* **2018**, *4*, 311−320.
(80) Shi, K.; Gu, K.; Shen, Y.; Srivastava, D.; Santiso, E. E.; Gubbins, K. E. High-Density Equation of State for a Two-Dimensional Lennard-Jones Solid. *J. Chem. Phys.* **2018**, *148*, 174505.
(81) Long, Y.; Śliwińska-Bartkowiak, M.; Drozdowski, H.; Kempiński, M.; Phillips, K. A.; Palmer, J. C.; Gubbins, K. E. High Pressure Effect in Nanoporous Carbon Materials: Effects of Pore Geometry. *Colloids Surfaces A Physicochem. Eng. Asp.* **2013**, *437*, 33−41.
(82) Long, Y.; Palmer, J. C.; Coasne, B.; Śliwinska-Bartkowiak, M.; Gubbins, K. E. Pressure Enhancement in Carbon Nanopores: A Major Confinement Effect. *Phys. Chem. Chem. Phys.* **2011**, *13*, 17163.
(83) van Dijk, D. Comment on "Pressure Enhancement in Carbon Nanopores: A Major Confinement Effect" by Y. Long, J. C. Palmer, B. Coasne, M. Śliwinska-Bartkowiak and K. E. Gubbins, Phys. Chem. Chem. Phys. , 2011, 13 , 17163. *Phys. Chem. Chem. Phys.* **2020**, *22*, 9824−9825.
(84) Long, Y.; Palmer, J. C.; Coasne, B.; Shi, K.; Śliwińska-Bartkowiak, M.; Gubbins, K. E. Reply to the 'Comment on "Pressure Enhancement in Carbon Nanopores: A Major Confinement Effect"' by D. van Dijk. *Phys. Chem. Chem. Phys.* **2020**, *22*, 9826−9830.
(85) Song, C. E.; Park, S. J.; Hwang, I.-S.; Jung, M. J.; Shim, S. Y.; Bae, H. Y.; Jung, J. Y. Hydrophobic Chirality Amplification in Confined Water Cages. *Nat. Commun.* **2019**, *10*, 851.

https://dx.doi.org/10.1021/acs.jctc.0c00607
J. Chem. Theory Comput. 2020, 16, 5548−5561